



1 **Application of anisotropy of magnetic susceptibility (AMS)**
2 **fabrics to determine the kinematics of active tectonics:**
3 **Examples from the Betic Cordillera, Spain and the northern**
4 **Apennines, Italy.**

5

6 David J. Anastasio¹, Frank J. Pazzaglia¹, Josep M. Parés², Kenneth P. Kodama¹, Claudio Berti³,
7 James A. Fisher¹, Alessandro Montanari⁴, Lorraine K. Carnes⁵

8

9 ¹ Department of Earth and Environmental Sciences, Lehigh University, Bethlehem, PA, 18015-3001, United States

10 ² Geochronology, Centro Nacional de Investigación de la Evolución Humana (CENIEH) Burgos, 09002, Spain

11 ³ Idaho Geological Survey, Moscow, ID, 83844-3014, United States

12 ⁴ Osservatorio Geologico di Coldigioco, Airolo MC, 62021, Italy

13 ⁵ Arizona State University, Tempe, AZ, 85281, United States

14

15 *Correspondence to:* David J. Anastasio (dja2@lehigh.edu)

16

17 **Abstract:** The anisotropy of magnetic susceptibility (AMS) technique provides an effective way to
18 measure fabrics and in the process, interpret the kinematics of actively deforming orogens. We collected rock fabric
19 data of alluvial fan sediments surrounding the Sierra Nevada massif, Spain, and a broader range of Cenozoic
20 sediments and rocks across the northern Apennine foreland, Italy, to explore the deformation fabrics that contribute
21 to the ongoing discussions of orogenic kinematics. Sierra Nevada is a regional massif in the hinterland of the Betic
22 Cordillera. We recovered nearly identical kinematics regardless of specimen magnetic mineralogy, structural
23 position, crustal depth, or time. The principal elongation axes are NE-SW in agreement with mineral lineations,
24 regional GPS geodesy, and seismicity results. The axes trends are consistent with the convergence history of the
25 Africa-Eurasia plate boundary. In Italy, we measured AMS fabrics of specimens collected along a NE-SW corridor
26 spanning the transition from crustal shortening to extension in the northern Apennines. Samples have AMS fabrics
27 compatible only with shortening in the Apennine wedge and have locked in penetrative contractional fabrics, even
28 for those samples that were translated into the actively extending domain. In both regions we found that specimens
29 have a low degree of anisotropy and oblate susceptibility ellipsoids that are consistent with tectonic deformation
30 superposed on compaction fabrics. Collectively, these studies demonstrate the novel ways that AMS can be
31 combined with structural, seismic, and GPS geodetic data to resolve orogenic kinematics in space and time.

32

33 **1 Introduction**

34 A number of *circum*-Mediterranean orogens are associated with rapid slab rollback, resulting in paired
35 compressional and extensional domains in the orogenic wedge of the retreating upper plate (Elter, 1975, Carminati
36 and Doglioni, 2012). Examples include, the Calabria Arc-Tyrrhenian Sea (Beccaluva et al. 1985; Milia et al 2009),
37 the Hellenic Arc-Aegean Sea (Pichon and Angelier 1979; Papazachos et al. 2000), and the Gibraltar Arc-Alboran
38 Sea (Lonergan and White 1997; Platt et al. 2006; Fernández-Ibáñez and Soto 2008). Along these tectonic
39 boundaries, the temporal and spatial relationship between thrust belt contraction, wedge-top basin evolution,



40 hinterland extension, and orogenic uplift are the subjects of continuing controversy.
41 Finite and incremental strain data provide deformation history and fabric distribution information for
42 kinematic studies of folds, faults, and orogens (e.g., Cloos, 1947; Ramsay and Huber, 1984; Fischer et al., 1992).
43 However, in orogenic forelands where deformation occurs at shallow depths and low temperatures, ductile
44 penetrative deformation features may be absent and brittle structures may be sparse. Anisotropy of magnetic
45 susceptibility (AMS) results offers an alternative proxy for grain preferred orientation, and hence rock strain, to
46 determine the tectonic fabric in these orogens where other deformation markers are not available (Borradaile and
47 Jackson, 2004; 2010; Borradaile and Henry, 1997; Averbuch et al., 1992; Pares, 2004). In general, comparative
48 studies from siliciclastic rocks show good agreement between both the relative magnitude and orientation of
49 penetrative rock strain determined by traditional geometric methods and AMS principal axes. The AMS axes in
50 specimens dominated by diamagnetic magnetic mineral abundance, the AMS axes orientations and not necessarily
51 the magnitude correlates to the rock strain. (e.g., Latta and Anastasio, 2007; Burneister et al., 2009). In this paper,
52 we show how AMS can extend the temporal reach of GPS geodesy and seismic first motion assessments back in
53 time in orogenic studies of the Betic Cordillera, Spain and in the northern Apennines, Italy (Fig. 1).
54

55 **2 Kinematic Studies For Active Tectonic Research**

56 Sedimentary rocks acquire a primary depositional fabric, which is bedding-parallel. It is measurable with
57 the AMS technique and is further enhanced and modified during burial, compaction, and water loss (e.g., Tarling
58 and Hrouda, 1993; Schwehr et al., 2006). Even unconsolidated rocks record a magnetic fabric that can potentially
59 provide a kinematic record (Mattei et al., 1997; Porreca and Mattei, 2012). The sensitivity of AMS allows its use
60 as a paleogeodetic tool in tectonic studies. Kinematics allow for an assessment of rheology and strain history that are
61 necessary prerequisites for understanding geodynamics, incrementally balancing cross sections, or in
62 paleogeographic reconstructions. We sampled both consolidated sedimentary rocks and unconsolidated sediments in
63 the Betic Cordillera, Spain and northeastern Apennine ranges, Italy for AMS analysis. The Betics field sampling was
64 designed to test AMS recovery from unburied and unconsolidated sediments around the Sierra Nevada massif. Here,
65 oriented samples were collected from sites at all structural positions around the Sierra Nevada massif in Plio-
66 Pleistocene terrestrial, siliciclastic deposits (Table A1). The Apennines field sampling was designed to measure the
67 rotation of strain across the foreland as rock passes from the actively shortening part of the orogenic wedge near the
68 trench to the actively extending regime further to the southwest. Here, oriented samples were collected from sites
69 along a NE-SW oriented corridor inclusive of Cenozoic (Table A1) marine and fluvial siliciclastics, marls, and
70 carbonate rocks, and unconsolidated Pleistocene fluvial sediments.
71

72 **3 The AMS Method**

73 The AMS ellipsoid is defined by the principal axes (k_1 -maximum, k_2 -intermediate, k_3 -minimum) of a specimen.
74 It can be represented by a second-rank tensor that characterizes a material's magnetization response to an applied
75 magnetic field (e.g., Borradaile and Tarling, 1981; Tarling and Hrouda, 1993). The orientation and relative length of
76 the principal anisotropy axes of a specimen are controlled by the preferred alignment of the anisotropy axes of the



77 individual magnetic particles in the specimen and the degree of the individual particle's anisotropy. The anisotropy
78 of individual magnetic grains is controlled by their crystallography and grain shape (Tarling and Hrouda, 1993). For
79 magnetite grains, the anisotropy is controlled by grain shape, whereas for hematite and phyllosilicate particles the
80 anisotropy is controlled by crystallography, which, in turn, controls their shape.

81 Natural processes such as current deposition, lithification, and tectonic deformation all contribute to a
82 specimen's AMS. In deformed rocks, it was shown that the principal susceptibility axis (k_1) orientation is typically
83 parallel to the strain long axis and orthogonal to the tectonic shortening direction, whereas the shortest axis (k_3), is
84 orthogonal to bedding in orientation (e.g., Kligfield et al., 1982; Hrouda, 1982), regardless of whether the individual
85 particle anisotropy is controlled by crystallography or shape.

86 The sedimentary rocks and deposits in this study contain enough phyllosilicate minerals to be excellent
87 specimens for AMS studies because of the presence of oblate mineral grains which adjust readily to deposition,
88 lithification, and any subsequent deformation. As grains reorient in response to depositional or tectonic processes,
89 the magnetic fabric will continuously adjust (Parés and van der Pluijm, 2002). Deposition from currents in alluvial
90 fans or rivers like the examples discussed here, will cause preferred grain alignment. Because the intermediate and
91 maximum AMS axes of platy grains, such as phyllosilicates, are nearly equal in magnitude they will be randomly
92 oriented in bedding, with the minimum axes orthogonal to bedding. In mudstones and fine grained sandstones,
93 where both paramagnetism and ferromagnetism contributions were quantified, paramagnetic mineral grains typically
94 dominate the AMS signal (Martin-Hernández and Hirt, 2001) because of the shape anisotropy of clay minerals,
95 although very fine magnetic particles attached to the clay fabric might also contribute (Kodama and Sun, 1992).

96

97 **4 Example I: Sierra Nevada Massif, Spain**

98 **4.1 Geologic Setting of Sierra Nevada Massif**

99 The Sierra Nevada massif is part of the Betic Cordillera-Rif-Tell orogens that extend along the European-
100 African plate boundary from the southern Iberian peninsula to northern Africa. These orogens are formed by slab
101 rollback and western migration of the Gibraltar Arc throughout the Neogene (Rosenbaum et al., 2002). Coincident
102 with the translation of the arc, the upper plate experienced shortening, the growth of doubly-vergent thrust belts,
103 crustal thickening, and rock uplift (Duggen et al., 2003; Soto et al., 2008; Platt et al., 2013). In the Betics,
104 contraction across the plate boundary was initially directed northward (Sanz De Galdeano, 1990; Lonergan, 1993;
105 Platt et al., 2013). As the contraction continued into the foreland during the late Miocene, it slowed and
106 progressively rotated to the northwest into its present orientation (Mazzoli and Helman, 1994; Rosenbaum et al.,
107 2002). Active tectonics in the Betic Cordillera today is dominated by distributed NW-SE convergence of 4-6 mm/yr
108 (Fernandez-Ibanez et al., 2007; Koulali et al., 2011; Gutshcer et al. 2012; Mancilla et al., 2013) and is
109 accommodated in part on NW-SE trending normal faults (Martínez- Martínez et al., 2006; Stich et al., 2006;
110 Fernández-Ibáñez and Soto, 2008; Giaconia et al., 2014; 2015; Fig. 2).

111 The Sierra Nevada massif is a doubly-plunging, actively uplifting (Azañón et al., 2015) elongate dome,
112 characterized by medium to low-grade metamorphic rocks stacked in north verging thrust sheets (Martínez-Martínez
113 and Soto, 2002). Previous interpretations are that the Sierra Nevada dome was uplifted following top to the west



114 extension and isostatic rebound after thrust belt formation (Martinez-Martinez et al., 2006). Alternatively, as many
115 culminations exist in orogenic hinterlands, the massif could have been uplifted during contractional or transpressive
116 strain (e.g., Bernini, 1990; Mitra et al., 1997).

117 To resolve whether the uplift of the Sierra Nevada dome was the result of extensional exhumation or a
118 compressional orogenic culmination, we collected rock fabric (AMS) data in Plio-Pleistocene deposits around the
119 massif to explore the presence of penetrative tectonic fabrics that can contribute additional constraints to the
120 kinematics of dome emplacement. We focused sampling on unburied alluvial fan deposits in Neogene basins that
121 surround the core of the structure (Fig. 3).

122

123 4.2 Methods for Example I

124 We collected samples from 6 sites distributed around Sierra Nevada, from all structural positions, around the
125 massif in unburied Plio-Pleistocene fan deposits that range from poorly cemented to unconsolidated (Sanz de
126 Galdeano and Vera, 1992; DR Table 1; Fig. 3). The ages of the deposits sampled were determined from published
127 geologic maps (IGME-1:50,000 scale) and bridged the temporal gap between the late Miocene age metamorphic
128 fabrics and the present day deformation field recorded by GPS geodesy and recent seismicity. At each site, three
129 oriented samples were collected as independent blocks. Before removal from the outcrop, most blocks were
130 hardened with a diluted (~50%) aqueous solution of sodium silicate (Fig. 4). In the laboratory, 2-3, oriented cubes
131 (8cm³) were cut from each block using non-magnetic Teflon knives and enclosed in standard cubic paleomagnetic
132 boxes. The anisotropy of magnetic susceptibility (AMS) was determined with an Agico Kappabridge KLY-3S at
133 Lehigh University. To determine magnetic mineralogy, a heating stage under the presence of an argon atmosphere
134 and a cold stage accessory to the Kappabridge was used.

135

136 4.3 Results for Example I

137 Results from heating and cooling experiments show a complicated magnetic mineralogy composed of 100%
138 ferromagnetic (magnetite or hematite) to 100% paramagnetic mineralogy (clays and iron-rich micas; Fig. 5). Since
139 the kinematic interpretation of each of the specimen is the same regardless of magnetic mineralogy, the details of
140 each specimen are not important for subsequent analysis. There is no correlation between the bulk magnetic
141 susceptibility (k_m) and the anisotropy of the magnetic ellipsoid (P_j), so a comparison of the principal axis of
142 susceptibility across the various structural positions around the Sierra Nevada massif specimens can provide useful
143 kinematic information (Fig. 6a). Nearly all AMS ellipsoids are characterized by a low anisotropy degree (P_j) and
144 oblate ellipsoid shape (T) (Jelinek, 1981; Fig. 6b). The AMS axes determinations record nearly the same axis
145 orientations. At all sites around Sierra Nevada, k_3 is nearly orthogonal to bedding. The principal elongation axes
146 means is preferentially oriented NNE-SSW to NE-SW (Fig. 3). The orientation of the site mean magnetic
147 susceptibility axes, k_1 , is horizontal or very shallowly plunging to the NE or SW (Fig 3).

148

149 4.4 Discussion of Example I



150 The AMS principal axes show a consistency between sites (Fig. 3), so we combine the susceptibility axes
151 orientation data in Figure 7. These combined data suggest that during deposition the phyllosilicate grains were
152 oriented with their basal planes parallel or slightly imbricated to the depositional surface. Compaction during
153 dewatering and lithification amplified the initial oblate depositional fabric and was coincident with the formation of
154 the tectonic fabric. Regardless of the magnetic mineralogy of the specimens, a well-clustered minimum
155 susceptibility axis (k_3) is present, which we interpret as a compaction fabric in these sedimentary deposits. The
156 possibility of a primary depositional current fabric (imbrication) is unlikely because of an independent paleocurrent
157 study on clast imbrication at Site 3 and Site 4, which shows an eastward rather than westward transport direction
158 during deposition (Carrigan et al., 2018).

159 Irrespective of the structural position around the Sierra Nevada massif, all sites show a preferred orientation
160 of k_1 . The mean principal axis of maximum susceptibility is preferentially oriented at 030° - 210° (Figs. 7 and 8). We
161 interpret this as a tectonic fabric due to the tight clustering of k_1 and k_2 , the relationship between k_1 and strike of
162 dipping bedding at sites SN1, SN4, and SN6, and the lack of influence from sedimentary processes. In specimens
163 dominated by phyllosilicate grains it is difficult to create a strong lineation by aligning grain crystallographic axes,
164 however, an intersection lineation between slightly rotated clay grains orthogonal to a shortening direction has been
165 observed (Henry, 1997; Parés et al., 2007; Martín-Hermández and Ferré, 2007; Borradaile and Jackson, 2010). The
166 orientation of k_1 is consistent with the present day GPS velocity field, being oriented almost perfectly orthogonal to
167 the direction of convergence of the Betic Cordillera to stable Africa (Nubia; Fig. 2; Gutscher et al., 2012), in good
168 agreement with the mineral lineations recorded in the massif's core (Martinez-Martinez and Soto, 2002), and the
169 Neogene brittle extensional structures and recent seismicity (Mancilla et al., 2013) in the orogen (Fig. 2). Because of
170 the low strains and the orthogonal relationship between contractional and extensional principal directions it is not
171 possible to distinguish the uplift processes of the Sierra Nevada massif with our results. The AMS ellipsoid
172 orientations, mineralogical matching lineation from the core of the Sierra Nevada massif, the nearby GPS velocity
173 field, and recent fault slip, all have orientations consistent with the same strain field (Fig. 8). The principal
174 elongation direction is interpreted to have persisted across different structural levels from Miocene time to the
175 present (> 10 m.y.).

176

177 **5 Example II: Northern Apennines, Italy**

178 **5.1. Geologic Setting of the Northern Apennines**

179 The northern Apennines are an accretionary fold and thrust belt (Bally, et al., 1986) where crustal
180 deformation, rock uplift, and topographic growth result from the ongoing subduction of Adria beneath Europe
181 (Picotti and Pazzaglia, 2008; Carminati and Doglioni, 2012). The Apennine orogenic wedge initiated ~ 30 Ma along
182 the southern flank of the Alps (Le Pichon et al., 1971), and has grown at variable rates through the Neogene
183 deposition on the flux of mass imbricated from the subducting plate (Picotti and Pazzaglia, 2008). Rapid rollback of
184 Adria with respect to Europe results in retreat and stretching of the upper plate, forming a wide zone of back arc
185 crustal extension. The Apennine wedge started to become emergent ~ 4 Ma (Picotti and Pazzaglia, 2008) uplifting
186 and exposing paired compressional and extensional deformation fronts near the trench and in the hinterland



187 respectively, with the structural transition near the topographic culmination of the range (D'Agostino et al., 2001;
188 Carminati and Doglioni, 2012). Balanced cross-sections for the Apennines (Bally et al., 1986; Hill and Hayward,
189 1988) indicate ~130 to 150 km of subduction over the 30 m.y. history of the wedge, which indicates relatively slow
190 long-term rates at ~ 4 to 5 km/m.y. (4 – 5 mm/yr), similar to the GPS geodetic rates (Devoti et al., 2008; Caporali et
191 al., 2011; Bennett et al., 2012).

192 The northeastern Apennines, including the Umbria-Marche target region of this research, exposes
193 Mesozoic-early Cenozoic carbonates and middle-late Cenozoic mixed carbonate-siliciclastic rocks folded and
194 imbricated into northeast-vergent thrust sheets (Fig. 9). In Marche, these thrust sheets are located with carbonate
195 ridges and have inferred blind thrusts in their cores (Artoni, 2013). Further west in Umbria, the thrust sheets are
196 dissected by both east- and west-dipping high angle normal faults (Barchi et al., 1998; Fig. 9). Ongoing thrust
197 earthquakes beneath the Po Plain and Adriatic Sea (Pondrelli et al., 2006; Boccaletti et al., 2011) and normal-fault
198 sense earthquakes beneath the high Apennines (Lavecchia et al., 1994; Doglioni et al., 1999; Ghisetti and Vezzani,
199 2002; Chiaraluce et al., 2017) speak to concurrent shortening and extension in the wedge.

200 The paired deformation fronts in the northern Apennines  are convolved with an enigmatic, but active,
201 east-dipping (towards Adria), 14-15 km deep detachment called the Alto-Tiberina fault, that projects to the surface
202 west of the Apennine crest (Barchi et al., 1998; Pialli et al., 1998; Boncio et al., 2004; Chiaraluce et al., 2007; Eva et
203 al., 2014; Lavecchia et al., 2016; Fig. 9). This detachment is one of only a handful of low angle normal faults
204 globally that are demonstrably seismogenic (Hreinsdottir and Bennett, 2009; Valoroso et al., 2017), apparently in
205 contradiction to frictional fault reactivation theory that predicts that slip on low angle normal faults as extremely
206 unlikely (reviewed in Collettini, 2011). Most of the destructive seismicity in the high Apennines tends to nucleate
207 on west-dipping high angle normal faults that are antithetic to and sole into this east-dipping detachment (Galadini
208 and Galli, 2000; Boncio et al., 2004; Roberts and Michetti, 2004). The most destructive seismicity, including the
209 2016-17 earthquake sequence, is tightly focused along the highest crest of the Apennines where it is co-located with
210 young, underfilled, extensional basins, high angle normal faults that rupture the surface (Fig. 9), and geomorphic
211 evidence for an east-marching drainage divide. It is not known if the infrequent, but large historic earthquakes east
212 of the divide are indicative of new blind normal faults that have nucleated on the detachment, represent active
213 shortening, or alternatively are responding to a different stress field.

214 Imbricated foredeep and wedge-top basins contain a time-transgressive range of poorly consolidated
215 deposits that span the extensional and compressional regimes. Conceivably, shortening fabrics could be recorded in
216 lithofacies at the base of one of these basins when it was formed and filled in the shortening part of the wedge, only
217 to be superseded by stretching fabrics in overlying lithofacies as the basin was translated westward and into the
218 extending part of the wedge. Adriatic slope transverse rivers (Alvarez, 1999) traverse both the extending and
219 shortening parts of the wedge and contain Pleistocene alluvial deposits representing an AMS geodetic snapshot of
220 the current crustal strains. Published AMS data from the thrust belt shows strike-parallel (NE-SW and horizontal)
221 extension that is perpendicular to compression and shortening directions (Caricchi et al., 2016). To confirm these
222 data towards the southeast and to better locate the kinematic transition region between the contracting and extending



223 regions of the overlying Eurasian plate, we sampled AMS data in Oligocene and younger units, including
224 Quaternary deposits in a NE-SW oriented corridor across the thrust belt (Fig. 9).

225

226 5.2 Methods for Example II

227 Sampling in the Apennines was designed to identify the location of the modern extensional front. Field
228 collection and specimen preparation occurred like sample I from Spain, with unconsolidated samples being
229 hardened with sodium silicate before or just after orienting and removal from the outcrop (Fig. 4). We collected
230 samples from 17 sites from sedimentary rocks and poorly consolidated sediments from Late Eocene to late
231 Pleistocene age, with a focus on late Miocene-Pliocene argillaceous marine deposits (DR Table 1). The Italian
232 specimens were prepared and rock magnetic data was acquired in the Archeomagnetism Laboratory at CENIEH
233 (Spain). The AMS of the collected specimens was measured on a MFK1-FA Kappabridge (AGICO Instruments), a
234 fully automated inductive bridge, at a frequency of 976 Hz and a field of 200 A/m. Analysis software (Saphyr6, by
235 AGICO) creates a complete susceptibility tensor. Rock magnetic measurements included isothermal remanent
236 magnetization (IRM) acquisition experiments up to 1T and hysteresis curves to determine the relative contribution
237 of ferromagnetism and paramagnetism to the total susceptibility tensor. These experiments were carried out with a
238 Vibrating Sample Magnetometer (VSM; Micromag 3900).

239

240 5.3 Results of Example II

241 Samples from the Apennines have variable magnetic mineralogy and include a wider range of lithologies and
242 ages than the Betics sampling. Samples from sites AP2 and AP7 (Bisciaro Fm.) are dominated by diamagnetic
243 calcite and negative mean susceptibility, which precludes any meaningful analysis of the AMS axes orientations. At
244 most other sites, axes orientations were interpretable and the k_1 orientation is shown in Figure 10 for spatial
245 comparison. At 1T field, the magnetization was not fully-saturated, indicating the presence of hematite in addition to
246 lower coercivity magnetite as the dominant ferromagnetic components (Heller, 1978). Still, the bulk magnetic
247 susceptibility is dominated by paramagnetism as revealed by the hysteresis curves (Fig. 11). The contribution of
248 paramagnetism suggests that the measured magnetic fabric can be used as a proxy for phyllosilicate grain
249 preferred orientation, therefore, the AMS principal axes are indicators of the orientation of the strain axes orientation
250 (e.g., Soto et al., 2009).

251 Representative examples of AMS fabrics are shown in Figure 12. The mean susceptibility shows no positive
252 correlation with the shape parameter or anisotropy degree (T , P_j ; Figure 13). Similar to the data from Spain, the
253 AMS ellipsoids from the Italian specimens indicate low P_j values, revealing a low degree of grain shape preferred
254 orientation and low strains. The AMS axes distribution are particularly clear in specimens of the argillaceous and
255 semi-consolidated Pliocene Argille Azzurre Fm. At all sites, k_1 axes orientations are shown as a function of rock
256 formation, as well as the sites in which k_3 is perpendicular to bedding (Fig. 10). All interpretable specimens from the
257 Apennine Range samples, including the Pleistocene fluvial deposits, generate a site mean AMS fabric consistent
258 with contraction and shortening in the wedge.

259



260 5.4 Discussion for Example II

261 Irrespective of sample age, we interpret AMS ellipsoids that have the magnetic lineation in a NW-SE
262 orientation as recording contraction as this is the main trend of the fault traces and strike of bedding and topography
263 (Fig. 10). The k_1 axis orientation is orthogonal to the rock transport and crustal shortening directions as recorded in
264 GPS geodesy data and seismology (Fig. 9). A few sites do not provide interpretable kinematic results. The
265 calcareous marls of the Bisciaro Fm. (AP2, AP7) have a poorly formed AMS fabric. In these specimens, the mean
266 susceptibility is negative and dominated by diamagnetism, most likely calcite. The absence of a compactional fabric
267 in carbonate dominated specimens (AP2, AP7) likely indicates that these sediments lithified by cementation soon
268 after deposition.

269 In general, the distribution of the principal axes of the AMS ellipsoid does not significantly vary with
270 stratigraphic age or structural position. For example, the oldest specimens collected from Eocene-middle Miocene
271 marls and Pliocene siliciclastics rocks (AP6, AP14, AP17), uniformly show AMS fabrics consistent with
272 contractional deformation of the orogenic wedge (Fig. 10). Most importantly, sites collected from thrust structures
273 that are currently in an extending regime (AP11, AP12, AP13) implies that either the AMS fabrics were locked after
274 the original deformation due to the high strain required to rotate grain pairs, or that subsequent extension has not
275 affected the previous AMS fabric. (e.g., Larrasoña et al., 2004). The same is true for middle and late Miocene
276 siliciclastic deposits astride the Marche ridge (AP3, AP9) where the current orientations of crustal stresses from fault
277 and earthquake data are ambiguous. Pliocene and Pleistocene samples from near the toe of the orogenic wedge show
278 an orientation consistent with ongoing shortening (AP4, AP5, AP8). Wegmann and Pazzaglia (2009) also report
279 ongoing shortening in this region as evidenced by fluvial terrace folding above the Filottrano thrust, which we cross
280 at the location of AP4.

281 The kinematic transition zone in central Italy aligns with the topography, the seismicity (Pondrelli et al.,
282 2006) and the GPS geodesy (Bennett et al., 2012; Fig. 9). Our AMS data does not improve on the location of the
283 transition zone because of the lack of samples from Plio-Pleistocene deposits directly northeast of the drainage
284 divide (Fig. 10). Unfortunately, the one Pleistocene river terrace deposit northeast of the divide (AP10) has
285 indeterminate axes. As such, our AMS results are not able to support the idea that there is an apparent rotation of the
286 principal compressive stress between the Adriatic coast and the Marche ridge associated with wedge-scale pore-
287 pressure variations (Peacock et al., 2017). Furthermore, the AMS is unable to determine the stress field responsible
288 for the large historic earthquakes in the region between the drainage divide and the Marche Ridge. If earthquakes in
289 the region are related to blind normal faults with tips breaking up-section from the Alto-Tiburina detachment (Fig.
290 9), a possible rationale is that according to extensional critical wedge theory (Davis et al., 1983), a wedge with a
291 taper greater than some critical value is unable to slide over its basal detachment until sufficient wedge thinning on
292 connecting faults reduces the surface slope and wedge taper below the critical value (Xiao et al., 1991). Suitable
293 deposits do outcrop in this critical region, so additional field work and AMS analyses may yet bear light on this
294 problem.

295 296 6 Conclusions



297 The AMS technique provides an effective way to identify both modern and paleo-kinematics from
298 sediments and sedimentary rocks largely independent of the magnetic mineralogy of a specimen. Stratigraphically
299 controlled AMS measurements are a deep-time, paleogeodetic technique that can be combined with structural
300 geology, GPS geodesy, and seismic data to collectively describe the kinematics of active orogens and to better
301 understand the nature of seismic hazards. In both the Betic Cordillera (Example I) and northern Apennines (Example
302 II), weak but well-organized penetrative AMS fabrics were recovered from young unconsolidated and unburied
303 rocks that could not be analyzed with more traditional methods. In the Betic Cordillera we established a long-term
304 consistency to the strain field from the Late Miocene to the present from unburied, young deposits around Sierra
305 Nevada. For the northern Apennines all studied sites, regardless of site's stratigraphic age, ubiquitously record NW-
306 SE oriented k_1 axes orientations, irrespective of structural position. Contractional strains in the most southwest-
307 located samples are likely locked into the rocks and do not record superposed penetrative extension.  case, the
308 recovered magnetic fabric orientation successfully determined the kinematics of an area near the synorogenic
309 surface, in the still contracting orogen toe region.

310

311 Author Contribution

312 Anastasio, Parés, and Berti conceived  Spanish project and completed sampling, sample preparation,
313 measurement, and analyses. Anastasio and Pazzaglia conceived  Italian project. Anastasio, Pazzaglia,
314 Montanari, and Karnes completed the Italian sampling. Anastasio and Parés prepared the Italian specimens,
315 measured the samples, and analyzed the results. Anastasio, Pazzaglia, Fisher, Berti, and Kodama analyzed results
316 and drafted figures for the manuscript. Anastasio and Pazzaglia wrote the first draft of the manuscript and edited
317 each subsequent draft. Parés, Kodama, Berti, and Montanari edited multiple drafts of the manuscript. Anastasio
318 completed the final edits.

319

320 Competing Interests

321 The authors all declare that they have no conflict of interest.

322

323 Special Issue Statement

324 This paper is intended for the special issue on “Tools, data and models for 3D seismotectonics: Italy a key
325 natural laboratory” Rita De Nardis, Massimiliano Porreca, Ramon Arrowsmith, Luca De Siena, Beatrice Magnani,
326 Frank Pazzaglia, and Federico Rossetti, editors.

327

328 7 Acknowledgements

329 The authors thank Andrea Rodriguez Rubio, Alondra Jimenez Perez, Isabel Hernando Alonso of CENIEH
330 for laboratory assistance and the Association “Le Montagne di San Francesco” for logistical support during the
331 sampling campaign in the Umbria-Marche Apennines. Agico is acknowledged for Anisoft software and Lisa Tauxe
332 is thanked for PmagPy software  to analyze the AMS data presented here. Anastasio thanks CENIEH and Parés
333 for hosting his academic leave during the fall 2019 semester.



334

335 **8 References**

336 Alvarez, W. Drainage on evolving fold-thrust belts: a study of transverse canyons in the Apennines. *Basin Res*, 11,
337 267-284. 1999.

338

339 Artoni, A.: The Pliocene-Pleistocene stratigraphic and tectonic evolution of the central sector of the Western
340 Periadriatic Basin of Italy. *Mar and Petrol Geol*, 42, 82-106. 2013.

341

342 Averbuch, O., Delamotte, D. F., and Kissel, C.: Magnetic fabric as a structural indicator of the deformation path
343 within a fold thrust structure – a test case from the Corbieres (NE Pyrenees, France). *J Struct Geol*, 14, 461-474.
344 1992.

345

346 Azañón, J. M., Galve, J. P., Perez-Pena, J. V., Giaconia, F., Carvajal, R., Booth-Rea, G., Jabaloy, A., Vazquez, M.,
347 Azor, A., and Roldan, F. J.: Relief and drainage evolution during the exhumation of the Sierra Nevada (SE Spain): Is
348 denudation keeping pace with uplift? *Tectonophysics*, doi:10.1016/j.tecto.2015.06.015. 2015.

349

350 Balley, A. W., Burbi, L., Cooper, C., and Ghelardoni, R.: Balanced sections and seismic reflection profiles across
351 the central Apennines. *Mem Soc Geol Ital*, 35, 257-310. 1986.

352

353 Barchi, M., De Feyter, A., Magnani, M., Minelli, G., Pialli, G. and Sotera, B.: Extensional tectonics in the Northern
354 Apennines (Italy): evidence from the CROP03 deep seismic reflection line. *Mem Soc Geol Ital*, 52, 528–538. 1998.

355

356 Bartole, R. The north Tyrrhenian-northern Apennines post-collisional system: Constraints for a geodynamic model.
357 *Terra Nova*, 7, 7 – 30. 1995.

358

359 Basili, R. and Barba, S. Migration and shortening rates in the northern Apennines, Italy:
360 Implications for seismic hazard. *Terra Nova*, 19, 462 – 468. 2007.

361

362 Beccaluva, L., G. Gabbianelli, F. Lucchini, P.L. Rossi, and Savelli, C: Petrology and K/Ar Ages of volcanics
363 dredged from the Eolian seamounts: Implications for geodynamic evolution of the Southern Tyrrhenian Basin. *Earth
364 Planet Sc Lett* 74, 187– 208. doi:10.1016/0012-821X(85)90021-4. 1985.

365

366 Bennett, R. A., Serpelloni, E., Hreinsdottir, S., Brandon, M. T., Buble, G., Basic, T., Casale, G., Cavaliere,
367 A., Anzidei, M., Marjonovic, M., Minelli, G., Molli, G., and Montanari, A.: Syn-convergent extension
368 observed using the RETREAT GPS network, northern Apennines, Italy. *J Geophys Res*, 117, B04408,
369 doi:10.1029/2011JB008744. 2012.



- 370
- 371 Bernini, B.M. The role of transpression movements in the evolution of Neogene basins of the Betic Cordillera. *An*
372 *Tect*, 4 ISSN: 0394-5596. 1990.
- 373
- 374 Bice, D., Lacroce, M., McGee, D., and Montanari, A.: Late Pleistocene tectonic tilting of the Frasassi anticline
375 from offset stalagmites in the Grotta Grande del Vento (Marche, Italy), in Koeberl, C., and Bice, D.M., eds., 250
376 Million Years of Earth History in Central Italy: Celebrating 25 Years of the Geological Observatory of Coldigioco.
377 *Geo S Am S* 542, 447–457. [https://doi.org/10.1130/2019.2542\(25\)](https://doi.org/10.1130/2019.2542(25)). 2019.cb
378
- 379 Boccaletti, M., Corti, G., and Martelli, L. Recent and active tectonics of the external zone of the Northern
380 Apennines (Italy). *Int J of Earth Sci, (Geol Rundsch)*, 100, 1331-1348, DOI: 10.1007/s00531-010-0545-y. 2011.
381
- 382 Boncio, P., and Lavecchia, G. Pace, B. Defining a model of 3D seismogenic sources for Seismic Hazard
383 Assessment applications: the case of central Apennines (Italy). *J Seismol*, 8, 407–425. 2004.
384
- 385 Borradaile, G. J., and Jackson, M.: Anisotropy of magnetic susceptibility (AMS): magnetic petrofabrics of
386 deformed rocks, in Martín-Hernández, F. Lüneburg, C.M. Aubourg, and M. Jackson (eds.). *Magnetic Fabric:*
387 *Methods and Applications. Geo Soc Spec Publ*, 238, 299-360. London, 0305-8719/04/. 2004.
388
- 389 Borradaile, G. J., and Jackson, M.: Structural geology, petrofabrics and magnetic fabrics (AMS, AARM, AIRM). *J*
390 *Struct Geol*, 32, 1519–1551. doi: 10.1016/j.jsg.2009.09.006. 2010.
391
- 392 Borradaile, G. J., and Henry, B.: Tectonic applications of magnetic susceptibility and its
393 anisotropy. *Earth Sci Rev*, 4, 49-93. 1997.
394
- 395 Borradaile, G. J., and Tarling, D. H.: The influence of deformation mechanisms on magnetic fabrics in weakly
396 deformed rocks. *Tectonophysics*, 77, 151-168. 1981.
397
- 398 Burmeister, K. C., Harrison, M. J., Marshak, S., Ferre, E. C., and Bannister, R. A.: 2009. Comparison of Fry strain
399 ellipse and AMS ellipsoid trends to tectonic fabric trends in very low-strain sandstone of the Appalachian fold-thrust
400 belt. *J Struct Geol*, 9, 1028-1038. 2009.
401
- 402 Butler, R. F.: *Paleomagnetism : magnetic domains to geologic terranes*. Blackwell Scientific Publications, Boston.
403 1992.
404



- 405 Caporali, A., Barba, S., Carafa, M.M.C., Devoti, R., Pietrantonio, G., and Riguzzi, F.: Static stress drop as
406 determined from geodetic strain rates and statistical seismicity. *J Geophys Res*, 116, B02410.
407 doi:10.1029/2010JB007671. 2011.
- 408
- 409 Caricchi, C., Cifelli, F., Kissel, C., Sagnotti, L., and Mattei, M.: Distinct magnetic fabric in weakly deformed
410 sediments from extensional basins and fold-and-thrust structures in the Northern Apennine orogenic belt (Italy):
411 *Tectonics*, 35, 238-256, doi:10.1002/2015TC003940. 2016.
- 412
- 413 Carminati, E., and Doglioni, C.: Alps vs. Apennines: The paradigm of a tectonically asymmetric Earth. *Earth Sci*
414 *Rev*, 112, 67-96. 2012.
- 415
- 416 Carrigan, J. H., Anastasio, D. J., Berti, C., and Pazzaglia, F. J.: Post-Messinian Drainage
417 Reorganization in an Active Orogen, Betic Cordillera, Spain. *Geo Soc Am Abstracts with Programs*. 2018.
- 418
- 419 Cavinato, G.P. and DeCelles, P.: Extensional basins in the tectonically bimodal central Apennines fold-thrust belt,
420 Italy. Response to corner flow above a subducting slab in retrograde motion. *Geology*, 27, 955–958. 1999.
- 421
- 422 Chiaraluce, L., Chiarabba, C., Collettini, C., Piccinini, D., and Cocco, M.: Architecture and mechanics of an active
423 low-angle normal fault: Alto Tiberina Fault, northern Apennines, Italy. *J Geophys Res*, 112, B10310,
424 doi:10.1029/2007JB005015. 1999.
- 425
- 426 Chiaraluce, L. Barchi, M. R., Carannante, S., Collettini, C., Mirabella, F., Pauselli, C., and Valoroso, L. The role of
427 rheology, crustal structures and lithology in the seismicity distribution of the northern Apennines. *Tectonophysics*,
428 694, 2810-291. 2017.
- 429
- 430 Cloos, E.: Oolite Deformation in South Mountain Fold, Maryland. *Geo Soc Am Bull*, 58, 843-918. 1947.
- 431
- 432 Collettini, C.: The mechanical paradox of low-angle normal faults: Current understanding and open questions.
433 *Tectonophysics*, 510, 253-268. 2011.
- 434
- 435 D'Agostino, N., Jackson, J. A., Dramis, F., and Funicello, R.: Interactions between mantle upwelling, drainage
436 evolution and active normal faulting: an example from the central Apennines (Italy). *Geophys J Int*, 147, 475-497.
437 2001.
- 438
- 439 Davis, D., Suppe, J., and Dahlen, F. A.: Mechanics of fold-and-thrust belts and accretionary
440 wedges. *J Geophys Res*, 88 (B2),1153-1172. 1983.
- 441



- 442 Devoti, R., Riguzzi, F., Cuffaro, M., and Doglioni, C.: New GPS constraints on the kinematics of the Apennines
443 subduction. *Earth and Planet Sci Lett*, 273, 163–174. 2008.
444
- 445 Doglioni, C., Harabaglia, P., Merlini, S., Mongelli, F., Peccerillo, A.T., and Piromallo, C. 1999. Orogens and slabs
446 vs. their direction of subduction. *Earth Sci Rev*, 45, 167–208. 1999.
447
- 448 Duggen S., Hoernle, K., van den Bogaard, P., Rüpke, L., & Morgan, J.P.: Deep roots of the Messinian Salinity
449 Crisis. *Nature*, 422, 602–606. DOI: 10.1038/nature01553. 2003.
450
- 451 Elter, P., Giglia, G., Tongiorgi, M., and Trevisan, L.: Tensional and compressional area in the recent (Tortonian to
452 present) evolution of the Northern Apennines. *B Geofis Teor Appl*, 17, 3–18. 1975.
453
- 454 Eva, E., Solarino, S., and Boncio, P.: HypoDD relocated seismicity in northern Apennines (Italy) preceding the
455 2013 seismic unrest: seismotectonic implications for the Lunigiana-Garfagnana area. *B Geofis Teor Appl*, 55, 739–
456 754. 2014.
457
- 458 Fernández-Ibáñez, F., and Soto, J.I.: Crustal Rheology and Seismicity in the Gibraltar Arc (western Mediterranean).
459 *Tectonics*, 27. doi:10.1029/2007TC002192. 2008.
460
- 461 Fernandez-Ibáñez, F., Soto, J. I., Zoback, M. D., and Morales, J.: Present-day stress field in the Gibraltar Arc
462 (western Mediterranean). *J Geophys Res: Solid Earth*, 112 (B08404) doi:10.1029/2006JB004683. 2007.
463
- 464 Galadini, F. and Galli, P.: Active tectonics in the central Apennines (Italy) - input data for seismic hazard
465 assessment. *Nat Hazards*, 22, 225–270. 2000.
466
- 467 Ghisetti, F., and Vezzani, L.: Normal faulting, transcrustal permeability and seismogenesis in the Apennines (Italy).
468 *Tectonophysics*, 348, 155–168. 2002.
469
- 470 Giaconia, F., Booth-Rea, G., Martínez-Martínez, J. M., Azañón, J. M., Storti, F., and Artoni, A.: Heterogeneous
471 Extension and the Role of Transfer Faults in the Development of the Southeastern Betic Basins (SE Spain).
472 *Tectonics*, 33, 2467–89. doi:10.1002/2014TC003681. 2014.
473
- 474 Giaconia, F., Booth-Rea, G., Ranero, C.R., Gràcia, E., Bartolome, R., Calahorrano, A., Lo Iacono, C., Vendrell,
475 M.G., and Cameselle, A.L.: Compressional tectonic inversion of the Algero-Balearic basin: Latest Miocene to
476 present oblique convergence at the Palomares margin (Western Mediterranean). *Tectonics*, 34, 1516–1543.
477 <https://doi.org/10.1002/2015TC003861>. 2015.
478



- 479 Gutscher, M.A., Dominguez, S., Westbrook, G.K., Le Roy, P., Rosas, F., Duarte, J. C., Terrinha, P., Miranda, J.M.,
480 Graindorge, D., Gailler, A., Sallares, V., and Bartolome, R.: The Gibraltar
481 Subduction: A Decade of New Geophysical Data. *Tectonophysics*, 574-575, 72–91.
482 doi:10.1016/j.tecto.2012.08.038. 2012.
483
484 Heller, F.: Rockmagnetic studies of Upper Jurassic limestones from southern Germany. *J Geophys*, 44, 525-543.
485 1978.
486
487 Henry B.: The magnetic zone axis: a new element of magnetic fabric for the interpretation of magnetic lineation.
488 *Tectonophysics*, 271, 325—331. 1997.
489
490 Hill, K. and Hayward, A.: Structural constraints on the Tertiary plate tectonic evolution of Italy. *Mar Petrol Geol*, 5,
491 2 – 16. 1988.
492
493 Hreinsdóttir, S., and Bennett, R.A.: Active aseismic creep on the Alto Tiberina low-angle normal fault, Italy.
494 *Geology* 37, 683–686. <https://doi.org/10.1130/G30194A.1>. 2009
495
496 Hrouda, F.: Magnetic Anisotropy of Rocks and Its Application in Geology and Geophysics.
497 *Geophysical Surveys*, 5, 37-82. <http://dx.doi.org/10.1007/BF01450244>. 1982.
498
499 Jelinek, V.: Characterization of the magnetic fabric of rocks. *Tectonophysics*, 79, 63-67. 1981.
500
501 Kligfield, R., Owens, W. H., and Lowrie, W.: Magnetic susceptibility anisotropy, strain and progressive deformation
502 in Permian sediments from the Maritime Alps (France). *Earth Planet Sc Lett*, 55, 181–189. doi: 10.1016/0012-
503 821X(81)90097-2. 1981.
504
505 Kodama, K. P. and Sun, W-W.: Magnetic anisotropy as a correction for compaction-caused
506 paleomagnetic inclination shallowing. *Geophys J Int*, 111, 465-469. 1992.
507
508 Koulali, A., Ouazar, D., Tahayt, A. King, R. W., Vernant, P., Reilinger, R. E., McClusky, S.,
509 Mourabit, T., Davila, J. M., and Amraoui, N.: New GPS constraints on active deformation along the Africa-Iberia
510 plate boundary: *Earth Planet Sc Lett*, 308, 211-217. 2011.
511
512 Larrasoña, J.C., Pueyo, E.L., and Parés, J.M.: An integrated AMS, structural, paleo- and rock-magnetic study of the
513 Eocene marine marls from the Jaca-Pamplona basin (Pyrenees, N Spain); new insights into the timing of magnetic
514 fabric acquisition in weakly deformed mudrocks. *Magnetic Fabric: Methods and Applications* (Martín-Hernández,
515 F., Lüneburg, C.M., Aubourg, C. y Jackson, M. Eds.). *Geol Soc Sp Publ*, London, 238, 127-143. 2004.



- 516
517 Latta, D.K. and Anastasio, D.J.: Multiple scales of mechanical stratification and décollement fold kinematics, Sierra
518 Madre Oriental foreland, northeast Mexico. *Jof Struct Geol*, 29, 1241-1255. 2007.
519
520 Lavecchia, G., Adinolfi, G. M., Nardis, R., Ferrarini, F., Cirillo, D., Brozzetti, F., De Matteis, R., Festa, G., and
521 Zollo, A.: Multidisciplinary inferences on a newly recognized active east dipping extensional system in Central
522 Italy. *Terra Nova*, 29, 77-89. 2016.
523
524 Lavecchia, G., Brozzetti, F., Barchi, M., Menichetti, M., and Keller, J.V.: Seismotectonic zoning in east-central
525 Italy deduced from an analysis of the Neogene to present deformations and related stress fields. *Geol Soc Am Bull*,
526 106, 1107–1120. 1994.
527
528 Le Pichon, X., G. Pautot, J. M. Auzende, and Olivet, J. L.: La Mediterranee occidentale depuis l'oligocene; scheme
529 d'évolution: The western Mediterranean since the Oligocene; evolutionary scheme, *Earth Planet Sc Lett*, 13, 145 –
530 152. 1971.
531
532 Le Pichon, X. and Angelier, J.: The Hellenic arc and trench system: a key to the neotectonic
533 evolution of the eastern Mediterranean area. *Tectonophysics*, 60, 1-42. 1979.
534
535 Lonergan, L.: Timing and kinematics of deformation in the Malaguide Complex, internal zone of the Betic
536 Cordillera, southeast Spain. *Tectonics*, 12, 460-476 <https://doi.org/10.1029/92TC02507>. 1993.
537
538 Lonergan, L., and White, N.: Origin of the Betic-Rif Mountain Belt. *Tectonics*, 16, 504–22.
539 doi:10.1029/96TC03937. 1997.
540
541 Makris, J., Egloff, F., Nicolich, R., and Rihm, R.: Crustal structure from the Ligurian Sea to the Northern
542 Apennines-a wide angle seismic transect. *Tectonophysics*, 301, 305 – 319. 1999.
543
544 Mancilla, FdL., Stich, D., Berrocoso, M., Martín, R., Morales, J., Fernandez-Ros, A., Paez, R.,
545 and Perez-Pena, A.: Delamination in the Betic Range: Deep structure, seismicity, and GPS motion. *Geology*, 41,
546 307-310. 2013.
547
548 Martín-Hernández, F. and Hirt, A.M.: The anisotropy of magnetic susceptibility in biotite,
549 muscovite and chlorite single crystals. *Tectonophysics*, 367, 13-28. 2003.
550
551 Martín-Hernández, F. and Ferré, E.C.: Separation of paramagnetic and ferrimagnetic anisotropies. A review. *J*
552 *Geophys Res: Sol Ea* 112 (B3), <https://doi.org/10.1029/2006JB004340>. 2007.



- 553
- 554 Martínez-Martínez, J. M., Booth-Rea, G., Azañón, J. M., and Torcal, F.: Active transfer fault
555 zone linking a segmented extensional system (Betics, Southern Spain): Insight into heterogeneous extension Driven
556 by Edge Delamination. *Tectonophysics*, 422, 159–73.
557 doi:10.1016/j.tecto.2006.06.001. 2006.
- 558
- 559 Martínez-Martínez, J. M. and Soto, J. I.: Orthogonal folding of extensional detachments: Structure and origin of the
560 Sierra Nevada elongated dome (Betics, SE Spain). *Tectonics*, 21, doi:
561 10.1029/2001TC001283. 2002.
- 562
- 563 Mattei, M., Sagnotti, L., Faccenna, C., and Funiciello, R.: Magnetic fabric of weakly deformed clay-rich sediments
564 in the Italian peninsula: Relationship with compressional and extensional tectonics. *Tectonophysics*, 271, 107–122.
565 1997.
- 566
- 567 Mazzoli, S. and Helman, M.: Neogene patterns of relative plate motion for Africa-Europe:
568 some implications for recent central Mediterranean tectonics. *Geol Rund*, 83, 464–68. 1994.
- 569
- 570 Milia, A., Turco, E., Pierantoni, P. P., and Schettino, A.: Four-dimensional tectono- stratigraphic evolution of the
571 southeastern Peri-Tyrrhenian Basins (Margin of Calabria, Italy). *Tectonophysics*, 476, 41–56,
572 doi:http://dx.doi.org/10.1016/j.tecto.2009.02.030. 2009.
- 573
- 574 Mitra, G., and Sussman, A.J.: Structural evolution of connecting splay duplexes and their
575 implications for critical taper; an example based on geometry and kinematics of the Canyon Range culmination,
576 Sevier Belt, central Utah. *J Struct Geol*, 19, 503–521. 1997.
- 577
- 578 Papazachos, B. C., Karakostas, V. G., Papazachos, C. B., and Scordilis, E. M.: The geometry of the Wadati-Benioff
579 zone and lithospheric kinematics in the Hellenic arc. *Tectonophysics*, 319, 275–300. 2000.
- 580
- 581 Parés, J. M., Hassold, N. J. C., Rea, D. K., and van der Pluijm, B. A.: Paleocurrent directions from paleomagnetic
582 reorientation of magnetic fabrics in deep-sea sediments at the Antarctic Peninsula Pacific margin (ODP Sites 1095,
583 1101). *Mar Geol*, 242, 4, 261–269. 2007.
- 584
- 585 Parés, J. M. and van der Pluijm, B. A.: Evaluating magnetic lineations (AMS) in deformed rocks. *Tectonophysics*,
586 350, 283–298. 2002.
- 587
- 588 Parés, J.M.: How deformed are weakly deformed mudrocks? Insights from magnetic anisotropy. *Geol Soc Sp*, 238,
589 191–203. 2004.



- 590
591 Parés, J.M. and van der Pluijm, B.: Phyllosilicate fabric characterization by low temperature
592 anisotropy of magnetic susceptibility (LT-AMS). *Geophys Res Lett*, 29, 68-1-68-4. 2003.
593
594 Peacock, C. P., Tavernelli, E., and Anderson, M. W.: Interplay between stress permutations and overpressure to
595 cause strike-slip faulting during tectonic inversion. *Terra Nova*, 29, 61-70,
596 doi:10.1111/ter.12249. 2017.
597
598 Peters, C. and Dekkers, M. J.: Selected room temperature magnetic parameters as a function of mineralogy,
599 concentration and grain size. *Phys Chem Earth*, 28, 659-667. 2003.
600
601 Pialli, G., Barchi, M., and Minelli, G., (eds.): Results of the CROP 03 deep seismic reflection profile. *Mem Soc*
602 *Geol Ital*, 52, 647 pp. 1998.
603
604 Picotti, V. and Pazzaglia, F. J.: A new active tectonic model for the construction of the Northern Apennines
605 mountain front near Bologna (Italy). *J Geophys Res*, 113, B08412, doi: 10.1029/2007JB005307. 2008.
606
607 Platt J. P., Anczkiewicz R., Soto J. I., and Kelley S. P., Thirlwall, M.: Early Miocene continental subduction and
608 rapid exhumation in the western Mediterranean. *Geology*, 34, 981-984. 2006.
609
610 Platt, J. P., Behr, W. M., Johannesen, K., and Williams, J.R.: The Betic-Rif Arc and its orogenic hinterland: a review.
611 *Annu Rev Earth and Pl Sc*, 41, 313–357.
612 doi:10.1146/annurev-earth-050212-123951. 2013.
613
614 Pondrelli, S., Salimbeni, S., Ekstrom, G., Morelli, A., Gasperini, P. and Vannucci, G.: The Italian CMT dataset
615 from 1977 to the present. *Phys Earth Planet Int*, 159, 286–303, doi:10.1016/j.pepi.2006.07.008. 2006.
616
617 Porreca, M. and Mattei, M.: AMS fabric and tectonic evolution of Quaternary intramontane extensional basins in the
618 Picentini Mountains (southern Apennines, Italy): *Int J Earth Sci*, 101, 863-877. 2012.
619
620 Ramsay, J. G. and Huber, M. I.: *The Techniques of Modern Structural Geology*, Vol. 1. Academic Press, San
621 Diego. 1984.
622
623 Richter, C., van der Pluijm, B., and Housen, B.: The quantification of crystallographic preferred orientation using
624 magnetic anisotropy. *J Struct Geol*, 15, 113–116. 1993.
625



- 626 Roberts, G.P. and Michetti, A.M.: Spatial and temporal variations in growth rates along active normal fault systems:
627 an example from the Lazio-Abruzzo Apennines, central Italy. *J Struct Geol*, 26, 339–376. 2004.
628
- 629 Rosenbaum, G., Lister, G. S., and Duboz, C.: Reconstruction of the Tectonic Evolution of the Western
630 Mediterranean since the Oligocene. *Tectonophysics*, 359, 117-129. 2002.
631
- 632 Rovida, A., Locati, M., and Camassi, R.: The Italian earthquake catalogue CPTI15. *B Earthq Eng*, 18, 2953–2984.
633 2020.
634
- 635 Sagnotti, L., Speranza, F., Winkler, A., Mattei., and Funicello, R.: Magnetic fabric of clay sediments from the
636 external northern Apennines (Italy). *Phys Earth Planet Int*, 105, 73-93. 1998.
637
- 638 Sanz De Galdeano, C.: Geologic evolution of the Betic Cordilleras in the Western Mediterranean, Miocene to the
639 present. *Tectonophysics*, 172, 107-119. [https://doi.org/10.1016/0040-1951\(90\)90062-D](https://doi.org/10.1016/0040-1951(90)90062-D). 1990.
640
- 641 Sanz De Galdeano, C. and Vera, J. A.: Stratigraphic record and palaeogeographical context of the Neogene basins in
642 the Betic Cordillera, Spain. *Basin Res*, 4, 21–36. 1992.
643
- 644 Schwehr, K., Tauxe, L., Driscoll, N., and Lee, H.: Detecting compaction disequilibrium with anisotropy of magnetic
645 susceptibility. *Geochem, Geophy, Geosy*, 7, Q11002. doi: 10.1029/2006GC001378. 2006.
646
- 647 Soto, J.I., Fernandez-Ibanez, F., Fernandez, M., and Garcia-Casco, A.: Thermal structure of the crust in the
648 Gilbralter Arc: Influence on active tectonics in the western Mediterranean. *Geochem, GeophyGeosy*, 9,
649 <http://dx.doi.org/10.1029/2008GC002061>. 2008.
650
- 651 Soto, R., Larrasoana, J.C., Arlegui, L.E., Beamud, E., Oliva-Urcia, B., and Simón, J.L.: Reliability of magnetic
652 fabrics of weakly deformed mudrocks as a palaeostress indicator in compressive settings. *J Struct Geol*, 31, 512 -
653 522. 2009.
654
- 655 Stich, D., Serpelloni, E., Mancilla, F. d. L., and Morales, J.: Kinematics of the Iberia– Maghreb plate contact from
656 seismic moment tensors and GPS observations. *Tectonophysics*, 426, 295–317, doi:10.1016/j.tecto.2006.08.004.
657 2006.
658
- 659 Tarling, D.H. and Hrouda, F.: *The Magnetic Anisotropy of Rocks*. Chapman and Hall, London, UK. 1993.
660
- 661 Tauxe, L.: *Paleomagnetic Principles and Practices*. Kluwer Academic Publishers. Norwell,
662 MA. 2002.



663

664 Tarquini S., Vinci S., Favalli M., Doumaz F., Fornaciai A., Nannipieri L.: Release of a 10-m-resolution DEM for
665 the Italian territory: Comparison with global-coverage DEMs and anaglyph-mode exploration via the web,
666 Computers & Geosciences , 38, 168-170. doi: doi:10.1016/j.cageo.2011.04.018. 2012.

667

668 Wegmar  W. and Pazzaglia, F. J.: Late Quaternary fluvial terraces of the Romagna and
669 Marche Apennines, Italy: Climatic, lithologic, and tectonic controls on terrace genesis in an active orogen.
670 Quaternary Sci Rev, 28, 137-165. 2009.

671

672 Valoroso, L., Chiaraluce, L., Di Stefano, R., and Monachesi, G.: Mixed-mode slip behavior of the Alto Tiberina
673 low-angle normal fault system (Northern Apennines, Italy) through high-resolution earthquake locations and
674 repeating events. J Geophys Res: Sol
675 Ea, 122, 10,220-10,240. 2017.

676

677 Xiao, H-B., Dahlen, F. A., and Suppe, J.: Mechanics of extensional wedges. J Geophys Res, 96, 10,301-10,318.
678 1991.

679

680 **Figure Captions**

681

682 Figure 1. Topography and bathymetry of the western Mediterranean showing (a) the Betic orogen, southern Spain
683 and (b) the northern Apennine Mountains, Italy. Elevation data from GEBCO 30sec data.

684 https://www.gebco.net/data_and_products/gridded_bathymetry_data/

685

686 Figure 2. Geodetic, paleogeodetic, and earthquake focal mechanism data from southern Spain. Generalized geology
687 (from Azañon et al.,2015), focal mechanism solutions for normal faults (from Mancilla et al, 2013), mineral
688 lineations [short red lines] (from Martinez-Martinez and Soto, 2002), results from 10-years of observed velocity
689 GPS permanent [black arrows, with uncertainties] (from Gutscher et al., 2012), and campaign [yellow arrows and
690 uncertainties] (from Koulali et al., 2011), stations in an African (Nubia) fixed reference frame. SN = Sierra Nevada.

691 Bathymetry color depths as in Fig. 1. Elevation data from 30 m SRTM NASA JPL. NASA Shuttle Radar

692 Topography Mission Combined Image Data Set. 2014, distributed by NASA EOSDIS Land Processes DAAC,

693 <https://doi.org/10.5067/MEaSURES/SRTM/SRTMIMG003>.

694

695

696 Figure 3. Simplified geologic map showing sample sites around the Sierra Nevada massif, southern Spain. Lower
697 hemisphere stereographic projection of AMS determined principal axes, k₁-red squares, k₂, green triangles, k₃, blue
698 circles. Bedding orientation shown along with axes orientation uncertainties. Elevation data from 30 m SRTM



699 NASA JPL. NASA Shuttle Radar Topography Mission Combined Image Data Set. 2014, distributed by NASA
700 EOSDIS Land Processes DAAC, <https://doi.org/10.5067/MEaSUREs/SRTM/SRTMIMG03>.

701

702 Figure 4.

703 Examples of specimen collection from poorly cemented samples. (a) a sampling surface is carved in a massive
704 sandstone of the upper Miocene Laga Fm., northern Apennines (b) the same is done on a subhorizontal layer of a
705 poorly cemented, fine calcareous sandstone from an upper Middle Pleistocene fluvial terrace exposed in a wine
706 cellar at the Geological Observatory of Coldigioco, northern Apennines. Both samples were hardened with a dilute
707 sodium silicate solution. Three to four oriented blocks were collected from each sampling site. Samples were
708 oriented with a Brunton compass and located with a handheld GPS receiver, labeled, and photographed.

709

710 Figure 5. Magnetic mineralogy of Sierra Nevada specimens. (top) Low temperature (MS vs T)
711 measured on a KLY-3s Kappabridge. Data in red and paramagnetic modeling in green indicating the proportion of
712 the magnetic susceptibility carried by paramagnetic grains. Results from all measurements indicate that the magnetic
713 susceptibility of the Spanish samples varies from being dominated by paramagnetic to ferromagnetic mineral grains.
714 The kinematic interpretation is the same in all cases. (bottom) High temperature (MS vs T) measurements showing
715 heating from room temperature (20°C) to 700°C and subsequent cooling back to room temperature. All sites
716 show evidence of the ferromagnetic mineral magnetite (Curie Temperature of 580°C). A lower temperature phase is
717 indicated in site 5, possibly maghemite. Site 5 shows the formation of additional magnetite during heating because
718 of the much stronger susceptibility upon cooling. Heating curves are in red and cooling curves in blue.

719

720 Figure 6. (a) Plot of mean susceptibility (K_m) with respect to ellipsoid shape, (T). Oblate shapes are positive T
721 whereas prolate shapes are negative T. The specimens are color coded by site and consistent with Fig. 3. The lack
722 of correlation between ellipsoid shape and susceptibility strengthens the conclusions based on site comparisons we
723 present here. (b) Jelinek diagram of Sierra Nevada specimens color coded by site and consistent with Fig. 3. All AMS
724 measurements have low anisotropy (less than 12% P_j), and nearly all specimens are oblate ($T > 0$). T and P_j are
725 calculated as follows: if $n_1 = \ln(t_1)$, $n_2 = \ln(t_2)$, $n_3 = \ln(t_3)$, where t_1 , t_2 , and t_3 are the eigenvalues, then $T = (2n_2 - n_1 -$
726 $n_3) / (n_1 - n_3)$ and $P = \exp(\sqrt{2[(n_1 - n_{mean})^2 + (n_2 - n_{mean})^2 + (n_3 - n_{mean})^2]})$ and $n_{mean} = (n_1 + n_2 + n_3) / 3$

727

728 Figure 7. All Sierra Nevada massif AMS data. Lower hemisphere, stereographic projection of the principal axes of
729 susceptibility orientations for all specimens determined from AMS measurements in stratigraphic coordinates (Fig.
730 3). Arrows outside the stereonet periphery are parallel to the mean long axis (k_1) orientation. $k_1 = \text{Maximum axis}$,
731 $k_2 = \text{intermediate axis}$, $k_3 = \text{minimum axis}$.

732

733 Figure 8. Kinematic summary of AMS Example I. Comparison of paleogeodetic methods around the Sierra Nevada
734 massif, Spain illustrating the validity of AMS determined principal extension direction (k_1).

735



736 Figure 9. (a) Location map showing the topography, major known faults, large, historic earthquakes (from Boncio
737 et al., 1998) and GPS geodetic velocities (from Hreinsdottir and Bennett, 2009) in the northern Apennine research
738 corridor (gray shaded box). Elevation data from TINITALY 10 m DEM (Tarquini et al., 2012). Alto Tiberina
739 Fault (ATF), Ancona (A), Apiro (Ap), Arezzo (Ar), Ascoli Piceno (AP), Cagli (C), Camerino (Cm), Cascia (Ca),
740 Fabriano (F), Foligno (Fo), Gola di Frasassi (GdiF), Gubbio (G), Jesi (J), Macerata (M), Norcia (N), Osservatorio
741 Geologico Coldigioco (OGC), Perugia (P), Spoleto (S), Visso (V). (b) Inset regional map showing the plate
742 boundary and location of Fig 9a. (c) Synthetic cross section of the region in (a) projected to the X-X' line
743 (modified from Chiaraluce et al., 2017). Normal faults in black, thrust faults in red, top of Permo-Triassic
744 evaporites in blue, top of carbonates in green. (d) Photo of a commonly exposed bedrock fault scarp from the
745 Umbrian Apennines. Fault scarps are uncommon in most of Marche.

746

747 Figure 10. Results of AMS analysis in the northern Apennines over 1:10,000 simplified geology (from regione
748 Marche and Umbria, regione.marche.it; <http://dati.umbria.it/>) and topography. Elevation data from 30 m NASA JPL
749 NASA Shuttle Radar Topography Mission Combined Image Data Set. 2014, distributed by NASA EOSDIS Land
750 Processes DAAC, <https://doi.org/10.5067/MEaSURES/SRTM/SRTMIMG003>. Extensional earthquake data
751 compiled from Rovida et al. (2020). The presence of a tectonic fabric was determined by clustering of k_1
752 declinations outside of the expected compaction fabric. Axis certainty represents the percentage of specimens of the
753 total used to calculate a mean k_1 vector. Right Legend: 1. Holocene fill; 2. 1st order Quaternary Terrace (Qt1); 3.
754 2nd order Quaternary Terrace (Qt2); 4 3rd order Quaternary Terrace (Qt3); 5. Argille Azzurre Fm; 6. Scaglia Rossa
755 Fm; 7. Maiolica Fm; 8. Bisciario Fm; 9. Hypothesized position of the modern extensional front based on AMS
756 results; 10. Thrust fault; 11. Normal fault; 12. Alto-Tiberina detachment. ; 13. Drainage divide; 14. Large historic,
757 but pre-instrument earthquakes of unknown origin (see Fig. 9).

758

759 Figure 11. (a) Hysteresis curves for representative samples of the studied Apennine Range geologic formations (see
760 location in Fig. 10). Paramagnetic susceptibility clearly dominates all the specimens as revealed by the slope of the
761 loops. (b) Example of a specimen where the paramagnetic contribution has been removed in order to enhance the
762 ferromagnetic contribution (loop in black). (c) Example of a specimen where diamagnetism dominates the total
763 magnetic susceptibility.

764

765 Figure 12. Lower hemisphere stereographic projection of representative sites showing representative fabric patterns
766 in Quaternary deposits (a) and older rocks in the Apennine foreland (b), (c), and older rocks south of extensional
767 front (d). The orientation of bedding is shown when not horizontal.

768

769 Figure 13. (a) Plot of mean susceptibility (K_m) with respect to degree of anisotropy, (P_j) for the Apennine specimens.
770 The specimens are color coded by site. (b) Jelinek diagram of Apennine specimens, colored by site. All AMS
771 measurements consistent with low strains (P_j , degree of anisotropy) and nearly all specimens are oblate ($T > 0$). T



772 and P_j are calculated as follow $n_1 = \ln(t_1)$, $n_2 = \ln(t_2)$, $n_3 = \ln(t_3)$, where t_1 , t_2 , and t_3 are the eigenvalues, then
773 $T = (2n_2 - n_1 - n_3) / (n_1 - n_3)$ and $P = \exp(\sqrt{2[(n_1 - n_{\text{mean}})^2 + (n_2 - n_{\text{mean}})^2 + (n_3 - n_{\text{mean}})^2]})$ and $n_{\text{mean}} = (n_1 + n_2 + n_3) / 3$.
774



Table A1.

Sample	Lat	Long	Elevation (m)	Formation	Age	Composition and Texture
Spain						
SN1	37.04972	-3.64923	853	-	Quaternary	Siliciclastic silt
SN3	36.9539	-3.05758	555	-	Quaternary	Siliciclastic silt
SN4	36.95832	-2.99537	600	-	Neogene	Siliciclastic silt
SN5	37.26138	-3.73503	609	-	Neogene	Siliciclastic silt
SN6	37.00809	-2.56091	501	-	Neogene	Siliciclastic sand
SN7	37.22960	-3.11414	1037	-	Neogene	Siliciclastic sand
Italy						
AP1	43.34778	13.12132	462	Ghiaia Urbisaglia Fm	Early Pleistocene	Calcareous and siliciclastic silt
AP2	43.36193	13.09481	454	Bisciaro Fm	Early Miocene	Argillaceous marl
AP3	43.35226	13.11542	502	Laga Fm	Late Miocene	Argillaceous silty sand
AP4	43.42590	13.23293	217	Qt4 alluvium	Late Pleistocene	Calcareous and siliciclastic silt
AP5	43.46141	13.30483	126	Argille Azzurre Fm	Pliocene	Siliciclastic blue-gray silty clay
AP6	43.53607	13.59282	218	Scaglia Variegata Fm	Late Eocene	Argillaceous marl
AP7	43.55456	13.57438	215	Bisciaro Fm	Early Miocene	Argillaceous marl
AP8	43.40956	13.10795	425	Argille Azzurre Fm	Pliocene	Siliciclastic blue-gray silty clay
AP9	43.30225	13.02115	469	Fm Camerino (Laga Fm)	Late Miocene	Siliciclastic argillaceous sandy silt
AP10	43.40180	12.96773	223	Qt3 alluvium	Middle Pleistocene	Calcareous and siliciclastic silt
AP11	43.41049	12.58075	553	Marnosa Arenacea Fm	Middle Miocene	Siliciclastic argillaceous sandy silt
AP12	43.38627	12.56814	638	Marnosa Arenacea Fm	Middle Miocene	Siliciclastic argillaceous sandy silt
AP13	43.38261	12.56343	629	Bisciaro Fm	Early Miocene	Argillaceous marl
AP14	43.20721	13.00143	520	Scaglia Cinerea Fm	Oligocene	Siliciclastic and calcareous argillaceous sandy silt
AP15	43.24922	12.97616	406	Scaglia Cinerea Fm	Oligocene	Siliciclastic and calcareous argillaceous sandy silt
AP16	43.51872	12.72748	500	Scaglia Cinerea Fm	Oligocene	Siliciclastic and calcareous argillaceous sandy silt
AP17	43.56574	12.80247	421	Laga Fm	Late Miocene	Siliciclastic argillaceous sandy silt

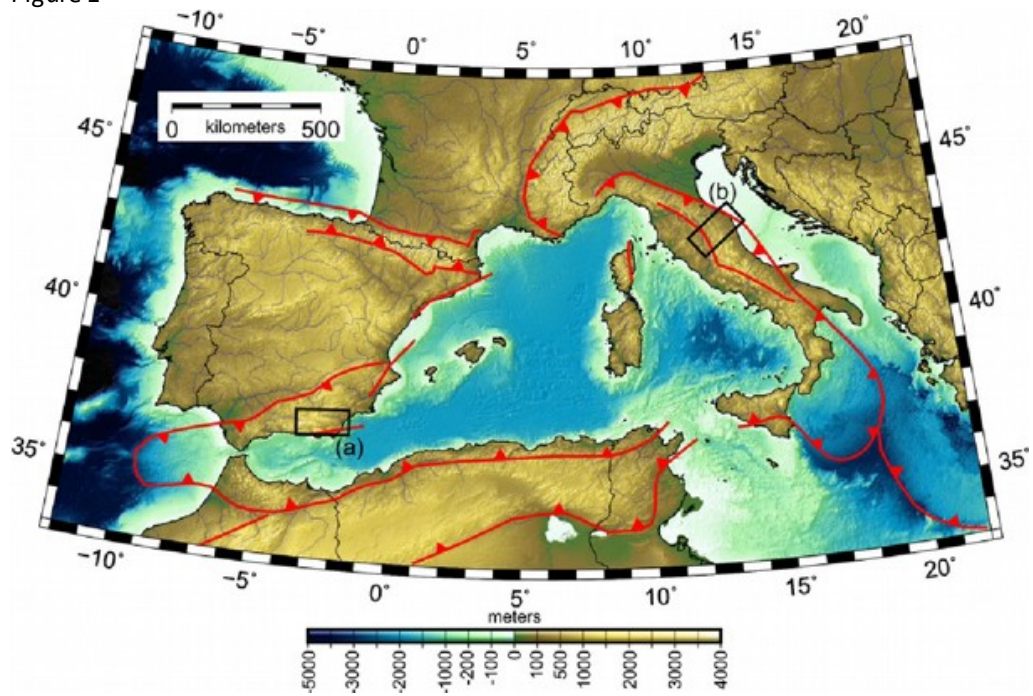
775
 776
 777



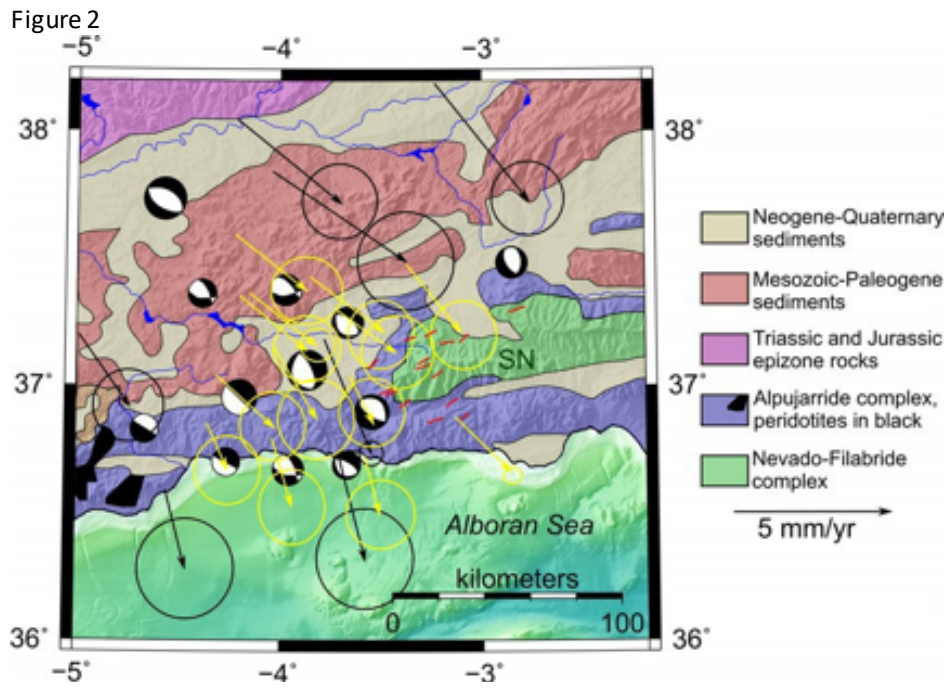
778

779

Figure 1



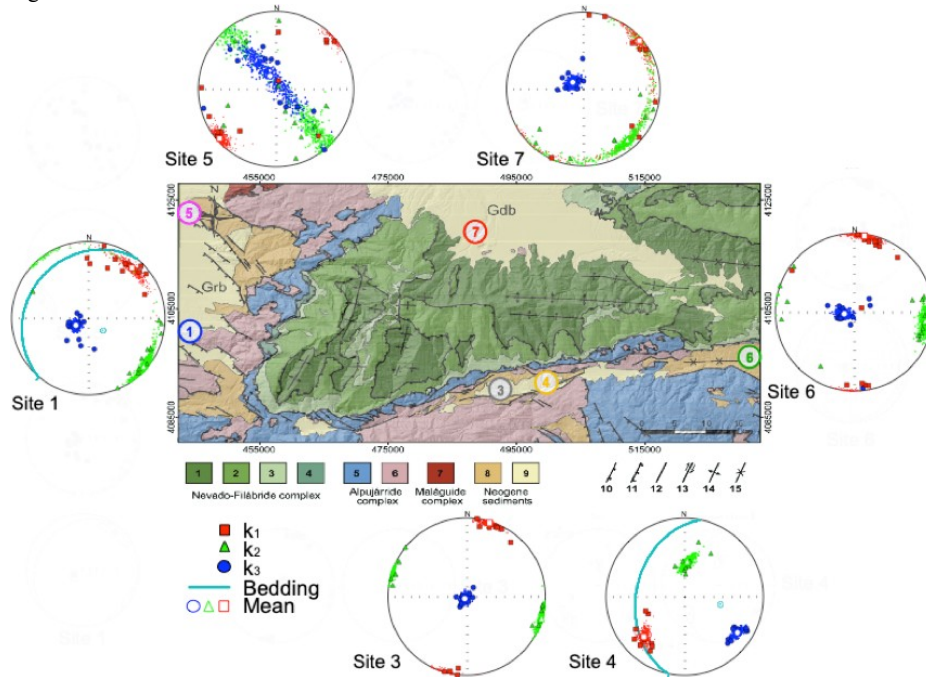
780
781



782
783



784 Figure 3



785
786
787
788
789
790
791
792
793



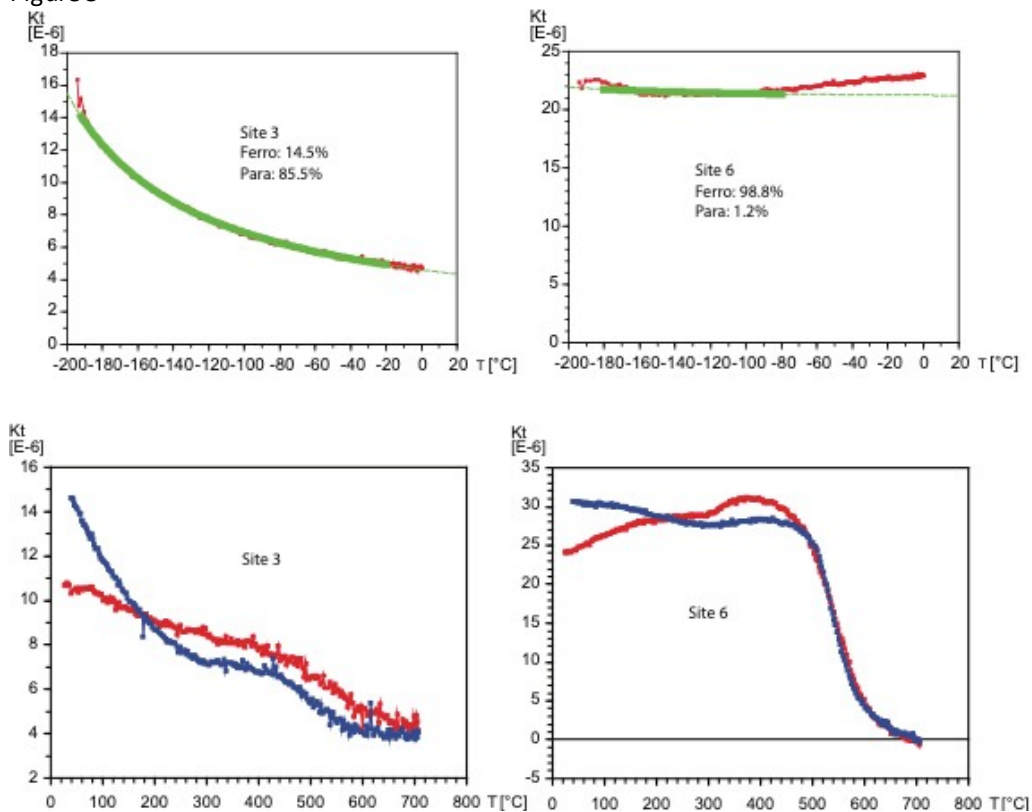
Figure 4



794
795
796
797



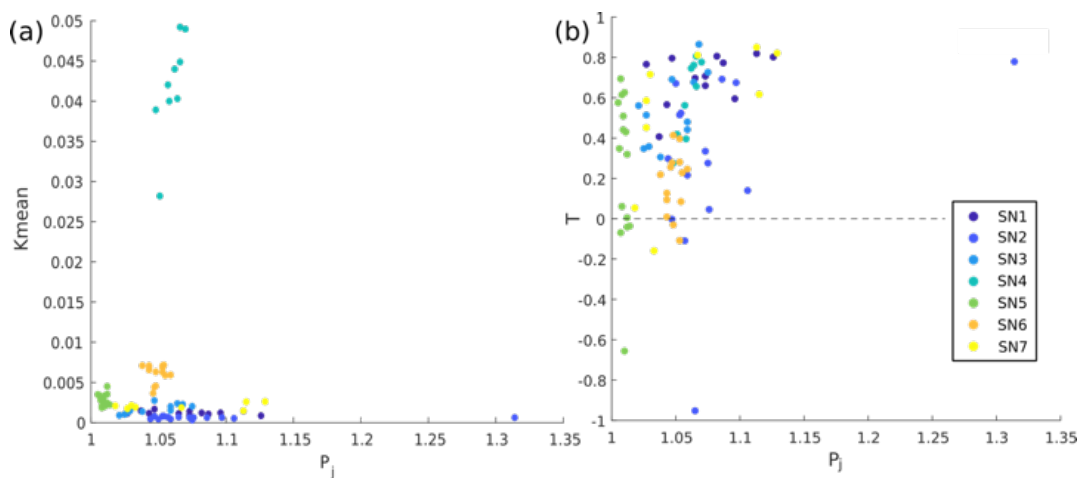
Figure 5



798
799
800



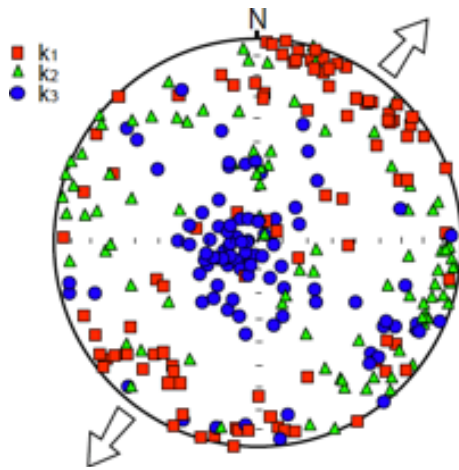
Figure 6



801
802
803
804



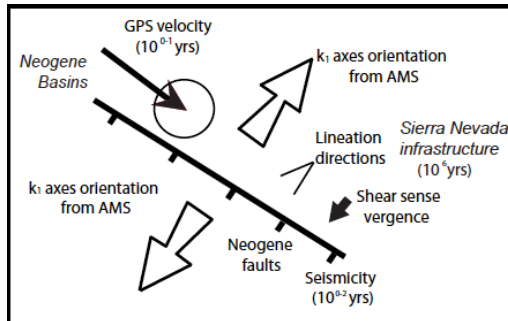
Figure 7



805
806
807
808



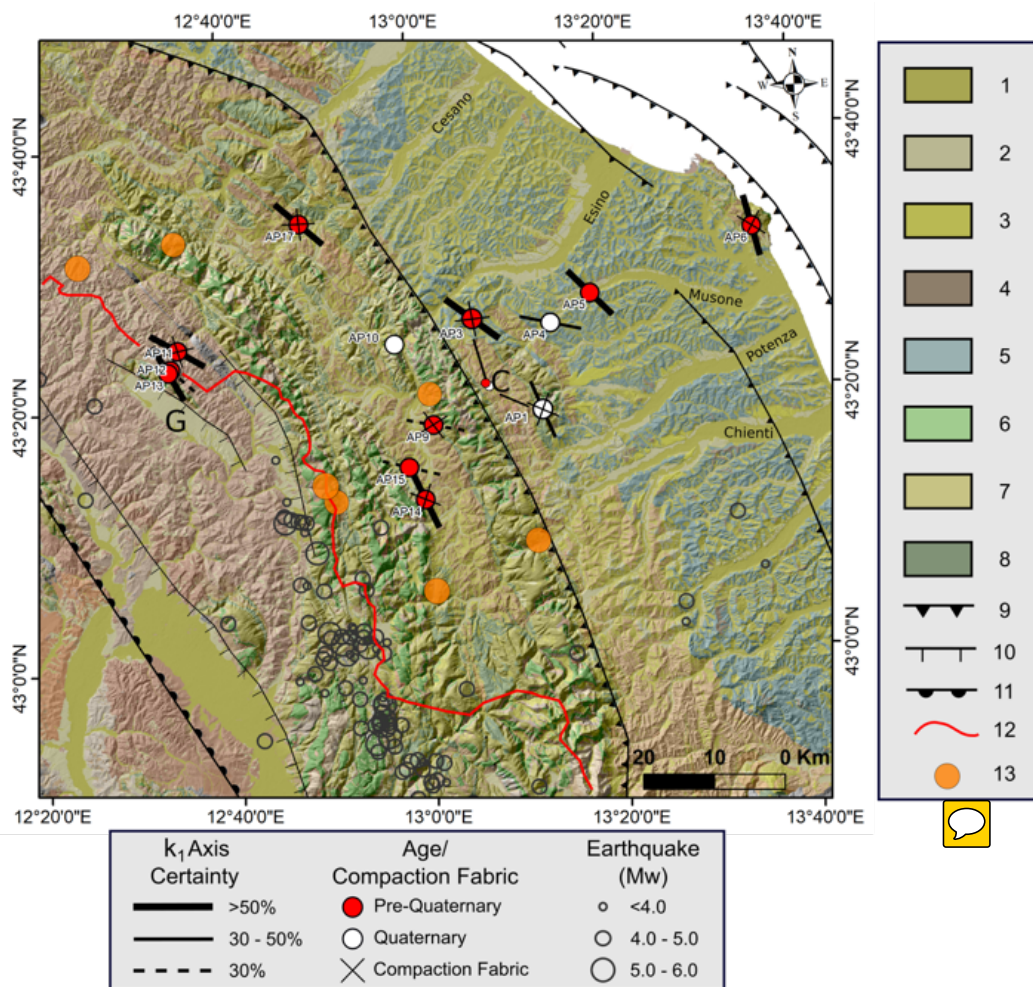
Figure 8



809
810
811
812
813
814
815
816



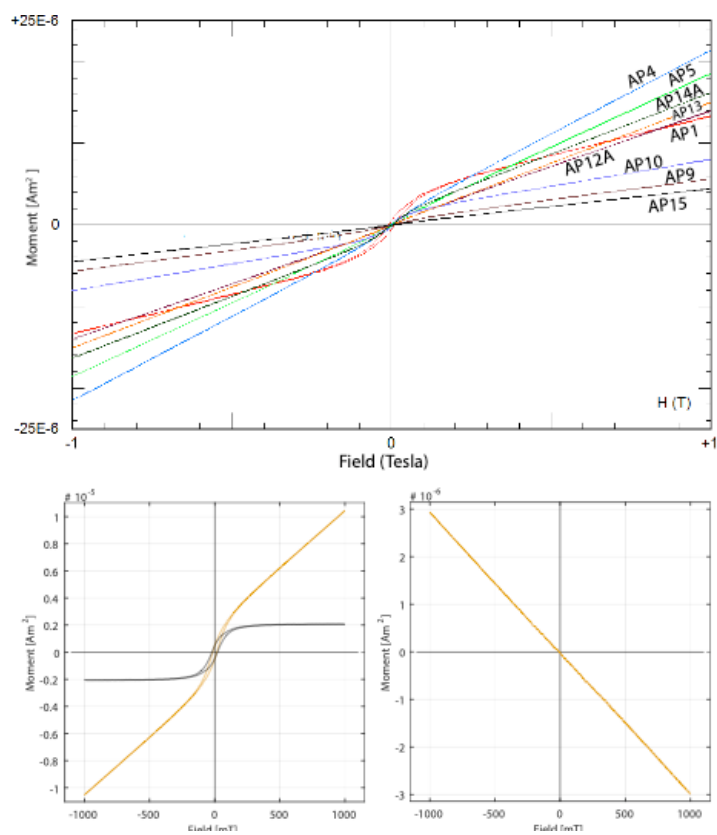
Figure 10



820
 821
 822
 823



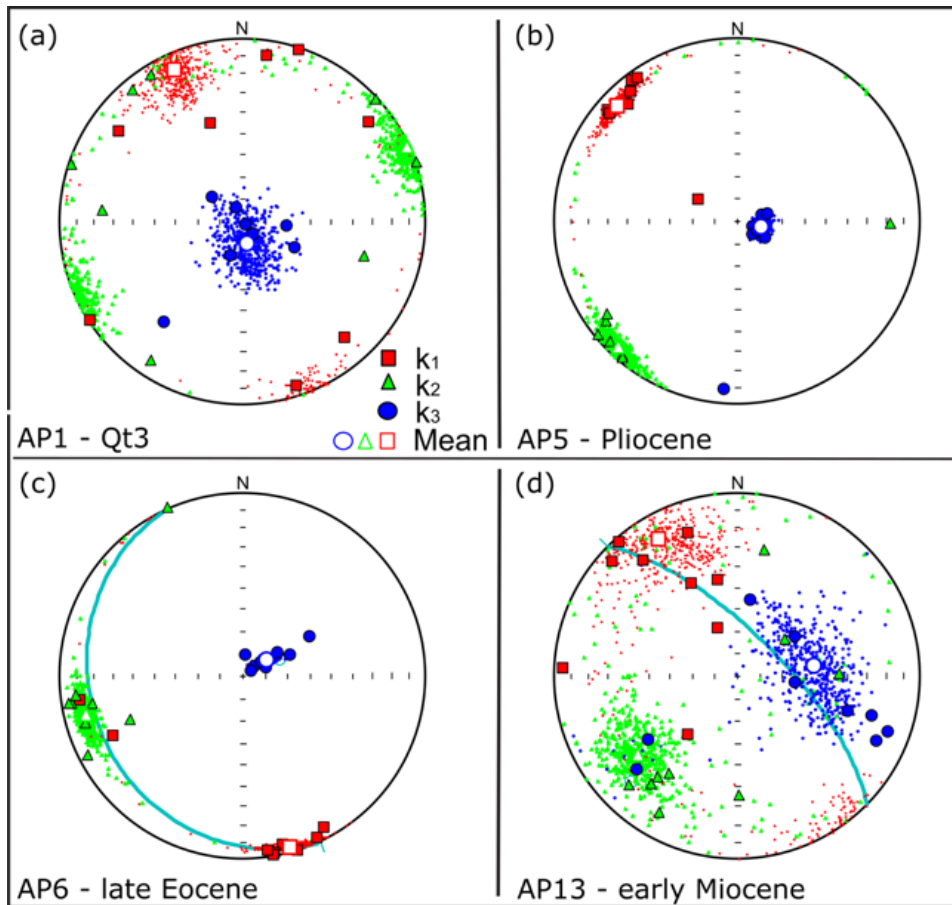
Figure 11



824
825
826



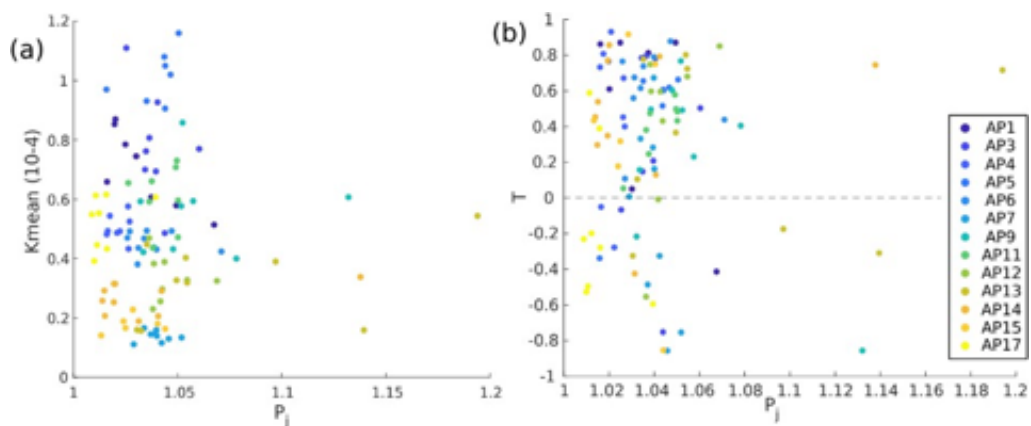
Figure 12



827
828
829



Figure 13



830
831